

See discussions, stats, and author profiles for this publication at: <https://www.researchgate.net/publication/231372327>

# Application of Coalescence and Breakup Models in a Discrete Bubble Model for Bubble Columns

ARTICLE *in* INDUSTRIAL & ENGINEERING CHEMISTRY RESEARCH · FEBRUARY 2005

Impact Factor: 2.59 · DOI: 10.1021/ie0492449

---

CITATIONS

35

---

READS

62

3 AUTHORS, INCLUDING:



Niels G Deen

Technische Universiteit Eindhoven

175 PUBLICATIONS 3,005 CITATIONS

SEE PROFILE



Hans A. M. Kuipers

Technische Universiteit Eindhoven

436 PUBLICATIONS 9,473 CITATIONS

SEE PROFILE

# Application of Coalescence and Breakup Models in a Discrete Bubble Model for Bubble Columns

E. I. V. van den Hengel,<sup>†,‡</sup> N. G. Deen,<sup>\*,†</sup> and J. A. M. Kuipers<sup>†</sup>

Faculty of Science and Technology, University of Twente, P.O. Box 217, 7500 AE Enschede, The Netherlands, and TNO Prins Maurits Laboratory, P.O. Box 45, 2280 AA Rijswijk, The Netherlands

In this work, a discrete bubble model (DBM) is used to investigate the hydrodynamics, coalescence, and breakup occurring in a bubble column. The DBM, originally developed by Delnoij et al. (*Chem. Eng. Sci.* **1997**, *52*, 1429–1458; *Chem. Eng. Sci.* **1999**, *54*, 2217–2226),<sup>1,2</sup> was extended to incorporate models describing the breakup and coalescence along with a subgrid scale closure model for the turbulence. To validate the turbulence model, simulation results of the DBM are compared to experimental PIV data of Deen et al. (*Chem. Eng. Sci.* **2001**, *56*, 6341–6350).<sup>3</sup> It is shown that incorporation of the subgrid scale model results in a better prediction of the mean and fluctuating velocity components in the bubble column, which can be subscribed to an increase of the effective viscosity. Furthermore, it was found that the predicted hydrodynamics are hardly altered when the subgrid scale velocity is taken into account in the evaluation of the interface forces. Finally, the bubble size distributions predicted by the DBM including the coalescence models of Chesters (*Trans. IchemE* **1991**, *69*, 259–270)<sup>4</sup> and Lee et al. (*Chem. Eng. Commun.* **1987**, *59*, 65–84)<sup>5</sup> are compared with experimental data that were obtained through digital image analysis in a pseudo 2D bubble column. It is found that the number of collisions between two bubbles that result in coalescence is 43% with the model of Chesters<sup>4</sup> and 85% with the model of Lee et al.<sup>5</sup> Coalescence occurs mostly in the lower part of the column. The mean diameter obtained from the DBM is higher than those measured experimentally, which is probably due to the lack of breakup.

## 1. Introduction

Many processes in the chemical industry involve contact of a dispersed gaseous phase and a continuous liquid phase. In these processes gas–liquid mass transfer takes place, often with accompanying chemical reactions. The specific interfacial area is a very important parameter for the rate of mass transfer and therefore the evolution of the bubble size distribution needs to be considered. Processes such as breakup and coalescence of bubbles have an enormous impact on the bubble size distribution and thus on the specific area and the mass transfer rate.

Detailed hydrodynamic models can give insight in the hydrodynamics of bubbly flows. Despite the widespread application of bubble columns and substantial research efforts devoted to understand their behavior, detailed knowledge on breakup and coalescence of bubbles is lacking and is often ignored in hydrodynamic modeling.

Flows in industrial bubble columns can be simulated using Euler–Euler or Euler–Lagrange models. The Euler–Euler models treat the different phases as continuous interpenetrating fluids. Contrary to the Euler–Euler model, the dynamics of individual bubbles are treated in the Euler–Lagrange model. In this type of model, also called discrete bubble model (DBM), a separate force balance is solved for each individual

bubble. This approach is very convenient for studying the behavior of the bubbles subject to breakup, coalescence, and mutual collisions. The incorporation of a bubble size distribution in this model is therefore straightforward. The downside of this model is that the number of bubbles is limited to about  $10^5$ . In addition, it requires substantial storage capacity and CPU time. In the Euler–Euler model the number of bubbles is not limited and storage requirements and demand of computer power depend on the number of computational cells considered, rather than the number of bubbles.

Sokolichin et al.<sup>6</sup> compared the result of the Euler–Euler and the Euler–Lagrange model. They noticed that the Euler–Euler approach can suffer from numerical diffusion. In the Euler–Lagrange model no numerical diffusion is introduced into the dispersed gas phase, because each bubble trace can be calculated accurately within a given volume element. They suggested the use of higher order discretisation schemes for the Euler–Euler model to reduce the numerical diffusion. When an appropriate discretization scheme is used, the Euler–Euler method provides results, which offer the same order of accuracy as the solution obtained with the Euler–Lagrange method. Sokolichin and Eigenberger<sup>7</sup> concluded this once more by comparing the results of the Euler–Euler model with the results of Delnoij et al.<sup>1</sup> Also Lapin and Lübbert<sup>8</sup> concluded that the Euler–Euler method is very sensitive to numerical diffusion and Euler–Lagrange methods perform much better in this respect.

Euler–Lagrange models for bubble columns were first used by Trapp and Mortensen<sup>9</sup> and Lapin and Lübbert.<sup>8</sup> The models developed by these authors differ in their description of the bubble dynamics and in the repre-

\* To whom correspondence should be addressed. Tel.: +31-53 489 4138. Fax: +31-53 489 2882. E-mail: N.G.Deen@utwente.nl.

<sup>†</sup> University of Twente.

<sup>‡</sup> TNO Prins Maurits Laboratory.

sensation of the coupling between the phases. Lapin and Lübbert<sup>8</sup> developed a 2D Euler–Lagrange model of a bubble column using a simple description of the bubble dynamics. Coupling between the gas and the liquid phases was achieved through the effective density of the mixture. No exchange of momentum between the phases was incorporated in their model.

In many DBM calculations turbulence of the continuous phase was not considered. Only an effective viscosity was used to match calculated results with measurements. Laín et al.<sup>10</sup> used the  $k$ – $\epsilon$  model to predict the flow in a bubble column. The values for the mean velocities showed reasonable agreement with PIV experiments for both phases, whereas the fluctuating velocity components were overpredicted. Laín et al.<sup>10</sup> found some problems in selecting the appropriate drag coefficient. The bubble rise velocity is considerably under-predicted compared to experimental results. This effect is the result of a reduced drag in a bubble swarm. Recently, Deen et al.<sup>3</sup> suggested the use of a subgrid scale model for the turbulence closure. They showed that when such a model is used, very good agreement could be obtained between an Euler–Euler model and experimental particle image velocimetry (PIV) data.

The Euler–Lagrange model needs closure relations to account for the interfacial forces. This information may be obtained from empirical relations or from simulations with more detailed models, such as volume of fluid or front tracking.<sup>11,12</sup>

In most numerical simulations of bubbly flows coalescence and breakup are neglected.<sup>1–3,7–12</sup> Only recently models for coalescence and breakup were incorporated in the Euler–Euler model<sup>13–15</sup> and the Euler–Lagrange model.<sup>16</sup> In the Euler–Euler model population balances are required to describe the bubble size distribution resulting from the bubble dynamics, and coalescence and breakup events. When the Euler–Lagrange method is used, these population balances are not required, due to the fact that each individual bubble is tracked in the system. When the bubble size distribution changes due to coalescence and breakup events, this is inherently captured by the model. Contrary to the work of Sommerfeld et al.<sup>16</sup> a deterministic bubble encounter model is used in our Euler–Lagrange model. In our work the liquid phase turbulence, breakup and coalescence are accounted for in the model and state of the art closures for the forces acting on bubbles are implemented. The hydrodynamics of the extended model have been validated for the case of a gas–liquid flow in a square cross-sectioned bubble column. Moreover, the model was used to simulate the hydrodynamics, coalescence and breakup in a flat bubble column. The predicted bubble size distributions are compared to experimental data.

## 2. Theoretical Model

The discrete bubble model consists of two coupled parts: a part describing the bubble motion and a part describing the liquid phase motion. The model requires constitutive equations for the forces acting on a bubble. The exchange of momentum between the gas and the liquid phase and vice versa is incorporated as a source term in the liquid phase momentum equation. The interaction between the bubbles is modeled via an encounter model, including bouncing, breakup and coalescence of bubbles.

**2.1. Bubble Dynamics.** The bubbles are tracked by solving an equation of motion for each individual bubble:

$$\rho_g V_B \frac{d\mathbf{v}}{dt} = \sum \mathbf{F} \quad (1)$$

The bubble dynamics are described by incorporating all relevant forces acting on a bubble rising in a liquid. It is assumed that the total force,  $\sum \mathbf{F}$  is composed of separate and uncoupled contributions originating from pressure, gravity, drag, lift, and virtual mass:<sup>17</sup>

$$\sum \mathbf{F} = \mathbf{F}_G + \mathbf{F}_P + \mathbf{F}_D + \mathbf{F}_L + \mathbf{F}_{VM} \quad (2)$$

The force acting on a bubble due to the gravity and pressure gradient, also called the buoyancy force, results in a net upward force.

The equation for the buoyancy force is given by

$$\mathbf{F}_{\text{Buoyancy}} = \mathbf{F}_G + \mathbf{F}_P = V_B(\rho_g \mathbf{g} - \nabla P) \quad (3)$$

The relation for the drag force acting on a sphere is given by eq 4. This force is proportional to the relative velocity between the bubble and the liquid ( $\mathbf{v} - \mathbf{u}$ ) and acts in the direction opposite to that of the bubble:

$$\mathbf{F}_D = -\frac{1}{2} C_D \rho_l \frac{1}{4} \pi d_B^2 |\mathbf{v} - \mathbf{u}| (\mathbf{v} - \mathbf{u}) \quad (4)$$

Tomiya<sup>18</sup> proposed three different closure relations for the drag coefficient  $C_D$ , which are valid for pure, slightly contaminated, and contaminated systems. These equations are based on a balance of forces acting on a single bubble rising in an infinite stagnant liquid and on available empirical correlations for the terminal rise velocities of single bubbles. In our model we used the relation for a pure system given by

$$C_D = \max \left[ \min \left[ \frac{16}{\text{Re}} (1 + 0.15 \text{Re}^{0.687}), \frac{48}{\text{Re}} \right], \frac{8}{3} \frac{\text{Eo}}{\text{Eo} + 4} \right] \quad (5)$$

The lift force consists of two parts: the classical shear-induced lateral lift force and the wake-induced lift force. Both forces act simultaneously on the bubble.

Auton<sup>17</sup> derived that the lift force is proportional to the cross product of the slip velocity and the curl of the liquid velocity. This implies that the lift force acts perpendicular to the path of the bubble.

$$\mathbf{F}_L = -C_L \rho_l V_B (\mathbf{v} - \mathbf{u}) \times \nabla \times \mathbf{u} \quad (6)$$

For small, spherical bubbles the lift coefficient  $C_L$  is equal to 0.5, whereas for large deformed bubbles the lift coefficient may become smaller and even negative due to the asymmetrical wake.<sup>18</sup>

The virtual mass force, also called the added mass force, is especially important in cases of unsteady rise when a bubble accelerates or decelerates, e.g., near the nozzle or in a turbulent flow field. The force can be seen as a resistance to acceleration, as the “added mass” of the liquid also has to be accelerated when the bubble accelerates. The virtual mass force can be represented as<sup>17</sup>

$$\mathbf{F}_{VM} = -\rho_l V_b C_{VM} \left( \frac{D_g \mathbf{v}}{Dt} - \frac{D_l \mathbf{u}}{Dt} \right) \quad (7)$$

The value of the virtual mass force is assumed to be independent of the void fraction and  $C_{VM}$  is taken equal to 0.5.

**2.2. Liquid Phase Hydrodynamics.** The liquid phase hydrodynamics are governed by the conservation equations for mass and momentum, respectively, given by

$$\frac{\partial(\alpha_l \rho_l)}{\partial t} + \nabla \cdot \alpha_l \rho_l \mathbf{u} = 0 \quad (8)$$

and

$$\frac{\partial(\alpha_l \rho_l \mathbf{u})}{\partial t} + \nabla \cdot \alpha_l \rho_l \mathbf{u} \mathbf{u} = -\alpha_l \nabla P - \nabla \cdot \alpha_l \tau_l + \alpha_l \rho_l \mathbf{g} + \Phi \quad (9)$$

The influence of the gas phase on the hydrodynamics of the liquid phase is expressed in two ways. The presence of the bubbles alters the liquid volume fraction  $\alpha_l$  and interface momentum transfer takes place due to action of the interface forces between the liquid and the bubbles. The latter is represented by the term  $\Phi$ :

$$\Phi = -\frac{1}{V_{\text{cell}}} \sum_{\forall i \in \text{cell}} (\mathbf{F}_{D,i} + \mathbf{F}_{L,i} + \mathbf{F}_{VM,i}) \quad (10)$$

The liquid phase stress tensor  $\tau_l$  is assumed to obey the general Newtonian form given by

$$\tau_l = -\mu_{\text{eff},l} \left( \nabla \mathbf{u} + (\nabla \mathbf{u})^T - \frac{2}{3} \mathbf{I} (\nabla \cdot \mathbf{u}) \right) \quad (11)$$

where  $\mu_{\text{eff},l}$  represents the effective shear viscosity, which is composed of three different contributions: the molecular viscosity, the turbulent viscosity, and the viscosity due to turbulence induced by the movement of the bubbles:

$$\mu_{\text{eff},l} = \mu_{L,l} + \mu_{T,l} + \mu_{\text{BIT},l} \quad (12)$$

There are several models available to take bubble-induced turbulence into account. In this study the model proposed by Sato and Sekoguchi<sup>19</sup> was adopted:

$$\mu_{\text{BIT},l} = \rho_l C_{\mu,\text{BIT}} \alpha_g d_B |\mathbf{v} - \mathbf{u}| \quad (13)$$

with the model constant  $C_{\mu,\text{BIT}} = 0.6$ .

Following the work of Deen et al.<sup>3</sup> the subgrid scale model of Smagorinsky<sup>20</sup> is used to calculate the turbulent viscosity  $\mu_{T,l}$ . This model represents the small-scale turbulent structures, which are smaller than the grid scale. The resulting turbulent viscosity is formulated as follows:

$$\mu_{T,l} = \rho_l (C_S \Delta)^2 |\mathbf{S}| \quad (14)$$

in which  $C_S$  is a constant with the value of 0.1,  $\mathbf{S}$  the characteristic filtered rate of strain and  $\Delta = (V_{\text{cell}})^{1/3}$  the filter width.

To incorporate the influence of the subgrid scale liquid velocity on the bubble dynamics, the following liquid velocity is used in the evaluation of the force balance:

$$\mathbf{u} = \mathbf{u}_{gs} + \mathbf{I} u_{\text{sgs}} \quad (15)$$

The subgrid scale part of the model is mimicked by a

uniform random, isotropic process with zero average and RMS value  $u_{\text{sgs}}$  given by

$$u_{\text{sgs}} = \sqrt{\frac{2}{3} k_{\text{sgs}}} \quad (16)$$

Each time step a new subgrid scale velocity is separately sampled for each bubble.

The subgrid kinetic energy  $k_{\text{sgs}}$  is calculated according to

$$k_{\text{sgs}} = C_k (C_S \Delta)^2 |\mathbf{S}|^2 \quad (17)$$

with  $C_k$  a constant with the value of 5.<sup>21</sup>

By combining eqs 14, 16, and 17, we obtain the following expression for the subgrid scale velocity:

$$u_{\text{sgs}} = \frac{\mu_{T,l}}{(C_S \Delta) \rho_l} \sqrt{\frac{2}{3} C_k} \quad (18)$$

**2.3. Coalescence and Breakup.** In our model encounters between a bubble and another bubble (binary encounter) and between a bubble and a solid wall are accounted for. Bubble–bubble and bubble–wall encounters are treated as ideal, frictionless hard-sphere collisions and have been computed using an event driven computational strategy employing efficient techniques (such as the neighbor list concept) taken from the field of molecular dynamics (MD) (see Delnoij et al.<sup>1,2</sup> for further details).

In this study, coalescence and breakup models were also included in the discrete bubble model. The coalescence rate is modeled as the product of the collision frequency  $\theta_C$  and, respectively, the coalescence efficiency  $P_C$ :

$$Q_C = \theta_C P_C \quad (19)$$

Contrary to Euler–Euler models, the DBM does not necessarily need closure for the collision frequency as it is a result of the collisions, which can be accounted for. The coalescence efficiency  $P_C$  is the probability that coalescence occurs after a collision between two bubbles with diameter  $d_a$  and  $d_b$  and depends on the exponent of the ratio of the coalescence time and the contact time:

$$P_C = \exp\left(-\frac{t_c}{\tau_c}\right) \quad (20)$$

In our work we adopted the coalescence models of Chesters<sup>4</sup> and Lee et al.<sup>5</sup> In the model of Chesters, the coalescence time is assumed to depend on the time to drain the film between two bubbles:

$$t_c \approx \frac{\rho_l |\mathbf{v} - \mathbf{u}| d_{ab}^2}{8\sigma} \quad (21)$$

where  $d_{ab} = 2(1/d_a + 1/d_b)^{-1}$  represents the equivalent diameter of bubbles a and b and  $\sigma$  is the surface tension. The contact time for bubbles is defined as

$$\tau_c = \left( \frac{\rho_l d_{ab}^3}{16\sigma} \right)^{(1/2)} \quad (22)$$

When eqs 21 and 22 are substituted in eq 20, the

following expression for the coalescence efficiency is obtained:

$$P_C = \exp\left(-\frac{1}{2}\sqrt{We}\right) \quad (23)$$

where the Weber number is defined as  $\{We\} = \rho_l(\mathbf{v} - \mathbf{u})^2 d_{ab}/\sigma$ .

In the model of Lee et al.<sup>5</sup> the coalescence time is equal to the time required for thinning plus the time of rupture:

$$t_c = \frac{d_{ab}}{8} \left( \frac{\rho_l d_{ab}}{2\sigma} \right)^{(1/2)} \ln\left(\frac{h_i}{h_f}\right) + 24\pi^2 M \sigma h_f^5 A_h^{-2} \quad (24)$$

where  $M = 0.034$  is the surface immobility parameter.  $h_i = 10^{-4}$  and  $h_f = 10^{-8}$  are respectively the initial and final thickness of the liquid film between the bubbles.  $A_h = 10^{-20}$  is the Hamaker constant.

The contact time is based on the theory of isotropic turbulence and is given by

$$\tau_c = \frac{(d_a + d_b)^{2/3}}{\epsilon^{1/3}} \quad (25)$$

where the energy dissipation is calculated on the basis of the turbulent viscosity:

$$\epsilon = \frac{2\mu_{T,l}^3}{(C_S \Delta)^4} \quad (26)$$

Breakup is described in a similar way as coalescence, where the event of breakup can be interpreted as the result of the interaction between a turbulent eddy with size  $\lambda_e$  and a bubble with size  $d_B$ . The breakup rate  $Q_{BU}$  is modeled as the product of the bubble–eddy collision rate  $\theta_{BU}$  and a breakup efficiency  $P_{BU}$ :

$$Q_{BU} = \int_{\lambda_{\min}}^{d_B} \theta_{BU} P_{BU} d\lambda_e \quad (27)$$

where  $\lambda_{\min}$  is the minimum eddy size that can break a bubble:

$$\lambda_{\min} = 11.4 \left( \frac{\nu_1^3}{\epsilon} \right)^{1/4} \quad (28)$$

The breakup model of Luo and Svendsen<sup>22</sup> is used in this work. In their model, the breakup efficiency is given by the probability that a bubble will break after it gets “hit” by a liquid phase eddy of size  $\lambda_e$ :

$$\theta_{BU}(V: f_{BV} V, \lambda_e) = \exp\left(-\frac{6d_B^2 \sigma (f_{BV}^{2/3} + (1 - f_{BV})^{2/3} - 1)}{\epsilon^{2/3} \lambda_e^{11/3}}\right) \quad (29)$$

where  $f_{BV}$  is the fractional volume of one of the daughter bubbles.  $f_{BV}$  is calculated with the following function, which has a U-shaped distribution, similar to the work of Luo and Svendsen:

$$f_{BV} = \frac{1}{2} + \frac{1}{2} \tanh(10(x - (1/2))/\pi) \quad (30)$$

where  $x$  is an evenly distributed random number between 0 and 1.

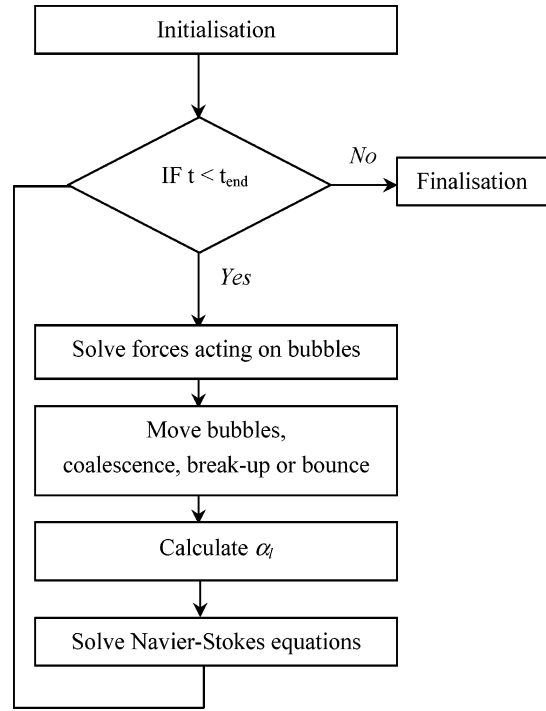


**Figure 1.** Computational flow diagram of the DBM.

The breakup efficiency is calculated as follows.

$$P_{BU}(\lambda_e) = 0.923(1 - \alpha_g) n_B \epsilon^{1/3} \frac{(d_B + \lambda_e)^2}{\lambda_e^{11/3}} \quad (31)$$

Finally, the substitution of eqs 29 and 31 in eq 27 yields the breakup rate.

### 3. Computational Method

In Figure 1, a computational flow diagram of the DBM is shown. After entering the main loop the forces acting on the bubbles present in the computational domain are computed and the bubbles are moved according to the Newtonian laws of motion. The encounter model is used to avoid bubbles to have overlap. Bubbles can bounce or coalesce, depending on the actual local conditions (radius of the bubble, approach velocity). When the bubbles are in a strong turbulent field, the bubbles can break. Bubbles leave the computational domain when they hit the top of the calculation domain.

The local liquid fraction is calculated from the position of the bubbles. As described previously the two-way coupling is achieved via the liquid volume fraction  $\alpha_l$  and the interface momentum transfer, represented by the term  $\Phi$ . Further details on the most recent improvements of the mapping of information between the Eulerian and Lagrangian phase and vice versa can be found in the work of Darmana et al.<sup>23</sup>

The Navier–Stokes equations are discretised on a staggered Eulerian grid. The incomplete Choleski conjugate gradient (ICCG) method is used to solve the pressure–Poisson equation. For the discretisation of the convection terms of the Navier–Stokes equation the second-order accurate Barton scheme is used.<sup>24–26</sup>

During the initialization step of the simulation, the pressure is set to the hydrostatic pressure in a quiescent liquid without bubbles. The boundary conditions required to solve the governing equations are incorporated using the flag matrix concept.<sup>27</sup> With this concept the



**Table 1. Cell Flags and Corresponding Cell Types Used in Defining Boundary Conditions**

flag	boundary condition
1	interior cell, no boundary condition specified
2	impermeable wall, free-slip boundary
3	impermeable wall, no-slip boundary
4	prescribed pressure cell, free-slip boundary
5	corner cell, no boundary condition specified

boundary conditions can be set for each individual computational cell (Table 1). At all the boundaries of the computational domain, except the top, no slip conditions were applied. For the top the free-slip boundary condition is used. At one grid cell from the top the column contains slits with prescribed pressure cells at all sides of the column. These slits occupy one-third of the top row of the column (see Figure 2).

#### 4. Experimental Procedure

The image analysis described in this section is used to measure the bubble size distribution and the mean diameter of bubbles in a pseudo 2D bubble at different heights in the column and at different superficial gas velocities. The size of the bubbles is determined by measuring the size of their shadows that are captured with the use of a digital camera. The image analysis is carried out with the VisiSize Solo software package from Oxford Lasers. A schematic overview of the experimental setup is shown in Figure 3.

A CCD camera generally records 8 bit images, which corresponds to 255 gray levels, ranging from black (0) to white (255). Only images with sufficient contrast between the gas and the liquid can be analyzed. When the column is illuminated from behind, the bubbles appear as dark objects on a light background. It is important for the analysis that the edges of the bubbles are dark and distinct from the background. However, light areas in the center of the bubble images will not affect the analysis. As is illustrated in Figure 4, the background can be identified as a broad peak at high gray levels in the gray level histogram of the recorded images. By only considering pixels with a gray level

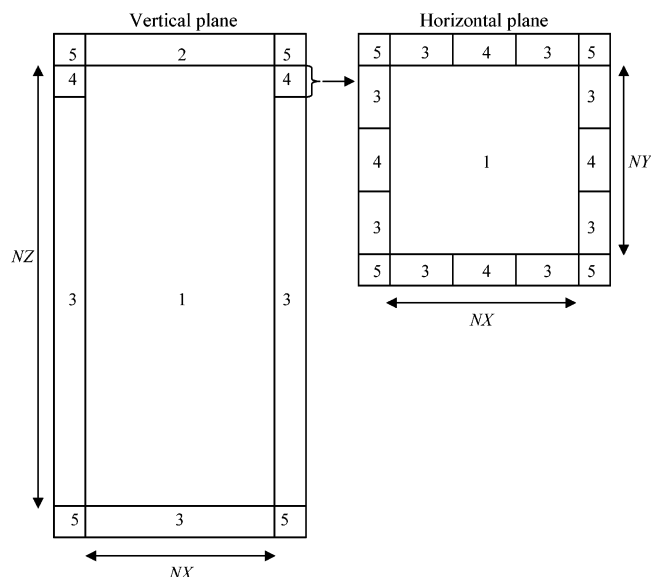


**Figure 2.** Typical boundary conditions used in simulations with the DBM (not to scale). The vertical plane is at  $j = NY/2$  whereas the horizontal plane is at  $k = NZ$ . The meaning of the cell flags is explained in Table 1.

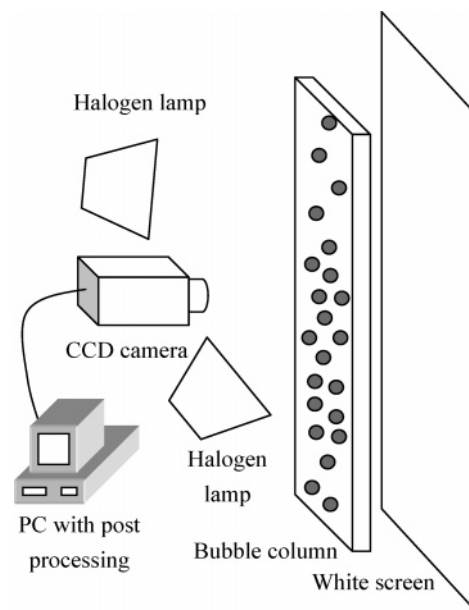


**Figure 3.** Schematic overview of the experimental setup for the measurement of the bubble size distributions in a pseudo 2D bubble column.

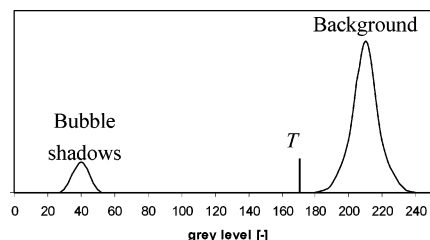


**Figure 4.** Typical gray level histogram for dark bubble shadows on a light background.

below a certain threshold  $T$ , the background can be removed from the image. The remaining signal originates from the shadows of the bubbles. It is essential to choose the value of the threshold carefully, to prevent removal of faint bubbles. After removal of the background, the size of each of the shadows is determined through a simple thresholded segmentation algorithm. The image is scanned from top to bottom, identifying dark segments on each line and associating them with the segments on the previous line. When a bubble is complete, calculations are performed on the bubble.

For circular bubbles the diameter calculation is straightforward. For noncircular shapes, there are several ways of characterizing the bubble size. In this work, the bubble diameter of a spherical bubble,  $d_A$  is determined which has an equivalent pixel area  $A_{\text{pixel}}$ :

$$d_A = C \sqrt{\frac{4A_{\text{pixel}}}{\pi}} \quad (32)$$

where  $A_{\text{pixel}}$  is the area of the bubble shadow and  $C$  is the magnification.

When the gas holdup in the column is larger than about 1%, the bubbles tend to overlap on the image. This could lead to the undesirable situation that a number of overlapping bubbles are interpreted as one large bubble. This could lead to a bias toward large bubble diameters. To prevent this situation from happening, all identified bubbles that differ too much from a spherical bubble are discarded. The sphericity can be

**Table 2. Overview of Different Simulation Cases for Hydrodynamics**

case	$\Delta x, \Delta y, \Delta z$ (mm)	$\Delta t_{\text{flow}}$ (s)	$\Delta t_{\text{bubble}}$ (s)	$\mu_{T,l}$	$\mu_{BIT,l}$	$u_{\text{sgs}}$
0	10	$1.0 \times 10^{-3}$	$1.0 \times 10^{-4}$	eq 14	0	eq 18
1	10	$5.0 \times 10^{-4}$	$5.0 \times 10^{-5}$	eq 14	0	eq 18
2	5	$1.0 \times 10^{-3}$	$1.0 \times 10^{-4}$	eq 14	0	eq 18
3	10	$1.0 \times 10^{-3}$	$1.0 \times 10^{-4}$	eq 14	0	0
4	10	$1.0 \times 10^{-3}$	$1.0 \times 10^{-4}$	0	0	0
5	10	$1.0 \times 10^{-3}$	$1.0 \times 10^{-4}$	eq 14	eq 13	eq 18

quantified as the ratio  $d_A/d_P$ , where  $d_P$  is the bubble diameter based on the pixel perimeter:

$$d_P = C \cdot \frac{P_{\text{pixel}}}{\pi} \quad (33)$$

It was found by using synthetic images that for a sphericity of more than 0.75 all overlapping bubbles were successfully removed, whereas most of the large bubbles were still detected correctly.

## 5. Results Hydrodynamics

The gas–liquid flow in a bubble column is modeled with the DBM as described in the previous sections. In this section the results of the simulations are discussed.

First the grid and time step dependence of the model are assessed. Next the results of the DBM with and without the subgrid scale turbulence model and subgrid scale velocity are discussed. The different computational cases are listed in Table 2.

Case 0 is used as a reference case for all other simulations. The results of this standard case are compared to experimental PIV results reported by Deen et al.<sup>3</sup> The bubble column used by Deen et al.<sup>3</sup> had a square cross section of  $0.15 \times 0.15 \text{ m}^2$  and a height of 1 m. The column was filled with distilled water up to an initial liquid height of 0.45 m. Air was introduced into the column through a perforated plate. The plate contained 49 holes, with a diameter of 1 mm, which were positioned in the middle of the column at a square pitch of 6.25 mm. The superficial gas velocity was 4.9 mm/s, corresponding to a gas flow rate of  $2.25 \times 10^{-6} \text{ m}^3 \text{ s}^{-1}$  per hole.

In the simulations, the initial bubble diameter was set to a constant value of 4.0 mm. The computational domain consisted of  $15 \times 15 \times 45$  grid cells and the time step was  $1.0 \times 10^{-3} \text{ s}$ . In the reference case the subgrid scale turbulence model (turbulence viscosity  $\mu_{T,l}$ ) and the subgrid scale velocity are both taken into account.

Each case was simulated for 180 s and the time-averaged mean velocity and the velocity fluctuations were calculated starting from 20 s. The time-averaged

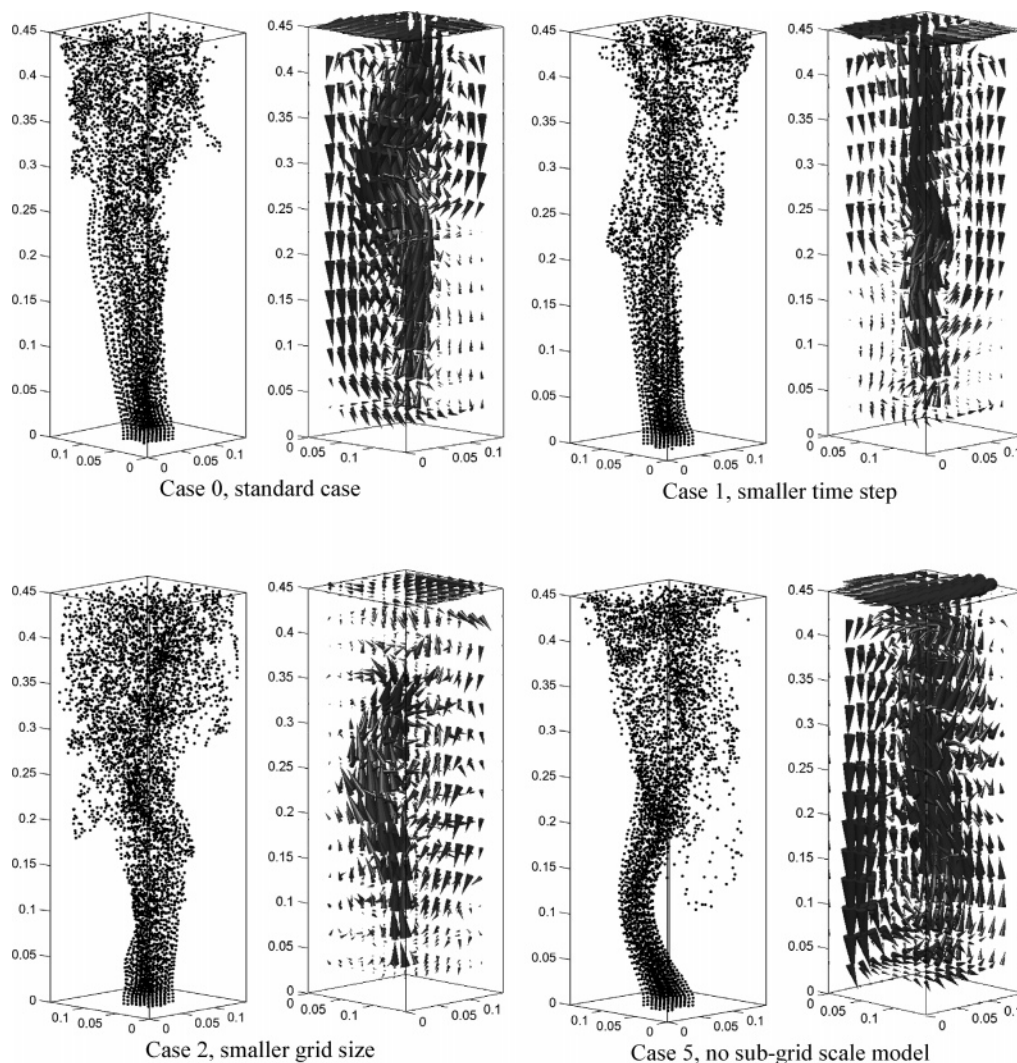


**Figure 5.** Snapshots of the bubble positions (left) and the liquid phase velocity (right) after 70 s for the different cases listed in Table 2.

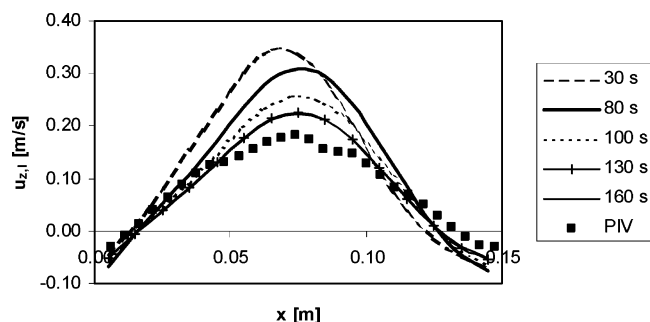


**Figure 6.** Comparison of the simulated and experimental average liquid velocity profiles for the standard case (see Table 2) at a height of 0.255 m and a depth of 0.075 m. Effect of the averaging period.

mean velocity is calculated as

$$\bar{u} = \frac{1}{N_t} \sum_{i=1}^{N_t} u_i \quad (34)$$

where  $N_t$  is the number of time steps used in the averaging.

The large-scale velocity fluctuations resolved by the model are calculated as follows:

$$u' = \frac{1}{N_t} \sqrt{\sum_{i=1}^{N_t} (u_i - \bar{u})^2} \quad (35)$$

In Figure 5 snapshots of the bubble positions and the liquid phase velocity are shown for cases 0, 1, 2 and 5. In all cases, the flow is driven by a bubble plume, which moves through the column in an oscillatory manner, which is in agreement with the experimental observations of Deen et al.<sup>3</sup> The observed trend is the same in all cases, although small differences exist. The differences can be attributed to the fact that small changes in the numerical settings will gradually lead to a different development of the flow. Whether these differences are significant can best be judged from a quantitative comparison of the time-averaged hydrodynamics.

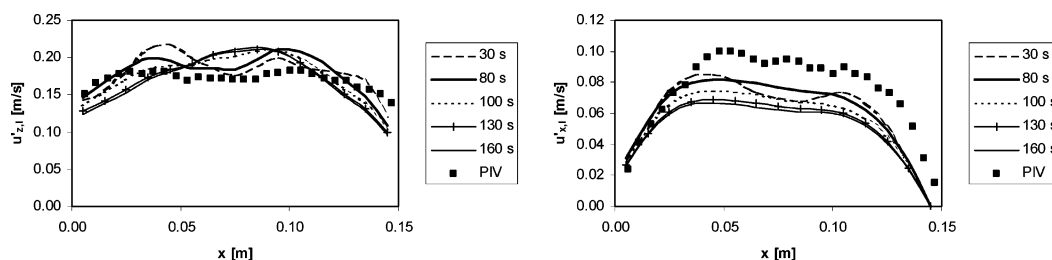


**Figure 7.** Comparison of the simulated and experimental average liquid velocity fluctuations for the standard case (see Table 2) at a height of 0.255 m and a depth of 0.075 m.

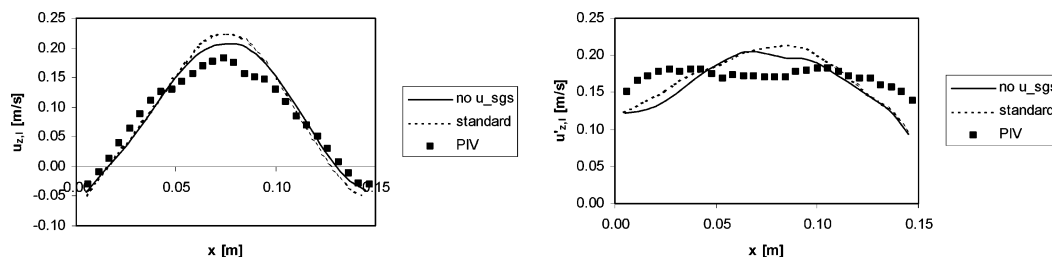


**Figure 8.** Comparison of the simulated and experimental average liquid velocity and velocity fluctuations for cases 0 and 3 (see Table 2) at a height of 0.255 m and a depth of 0.075 m. Effect of the subgrid scale velocity.

The simulations need to be carried out sufficiently long, to obtain statistically meaningful results. For this purpose, the average liquid velocity and velocity fluctuations after different averaging times are compared to the PIV results given in Figures 6 and 7, respectively. All the data appear to have converged after about 130 s.

It is found that the simulated average velocity is higher than the PIV results. This may be due to the underestimation of the lateral velocity fluctuations as shown in Figure 7. That is to say that if the bubble plume is less dynamic than in the experiments, this leads to less velocity variations as well as in increased liquid velocity in the center of the column, as most of the bubbles (and liquid) are rising in this region. However, the predicted vertical velocity fluctuations are in the right order of magnitude.

The time step and grid dependencies of the results were verified in cases 1 and 2, respectively. The differences with the standard case were found to be relatively small, which lead to the conclusion that the simulation results are nearly grid-independent.

**5.1. Turbulence Model.** The influence of the subgrid scale velocity (eqs 15 and 18) is investigated by comparing the standard case with case 3. It can be seen in Figure 8 that the results of the cases with and without the incorporation of the subgrid scale velocity are practically the same. Apparently the unresolved part of the liquid velocity can be neglected as compared to the resolved grid scale liquid velocity.

The influence of the turbulence model can be assessed by comparing cases 0 and 4. In case 4, both the turbulent viscosity and the subgrid scale velocity are set to zero. The results of both cases are shown in Figure 9. When the turbulence is taken into account, the effective viscosity is higher than when only the molecular viscosity is active. Low viscosities lead to less dampening of the bubble plume dynamics. Consequently, this leads to flatter average liquid velocity profiles, which are observed in Figure 9.

It appears that the vertical velocity fluctuations are less influenced by the choice of the turbulence model. The horizontal velocity fluctuations are more pro-



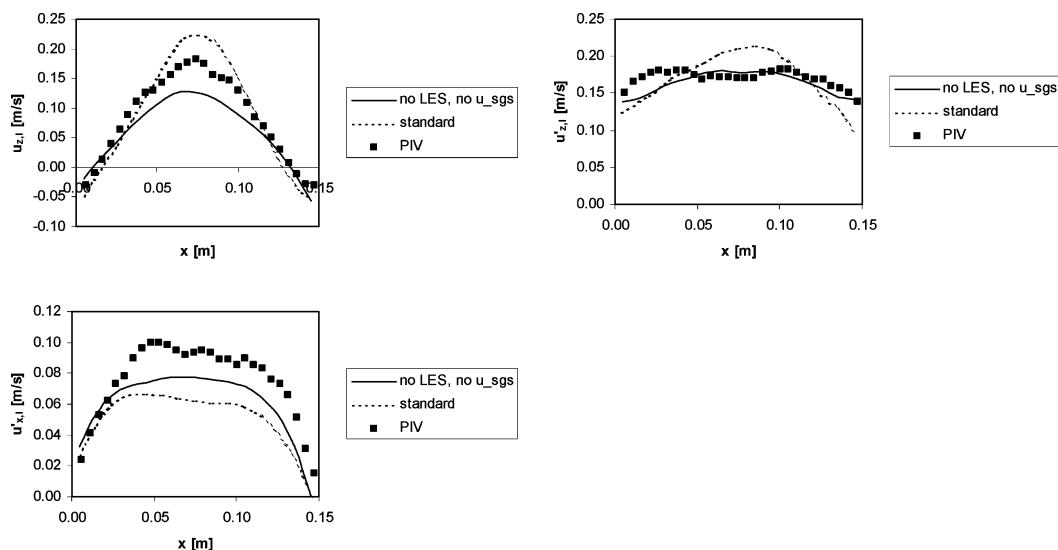


**Figure 9.** Comparison of the simulated and experimental liquid velocity and velocity fluctuations for cases 0 and 4 (see Table 2) at a height of 0.255 m and a depth of 0.075 m: Effect of the subgrid scale model.

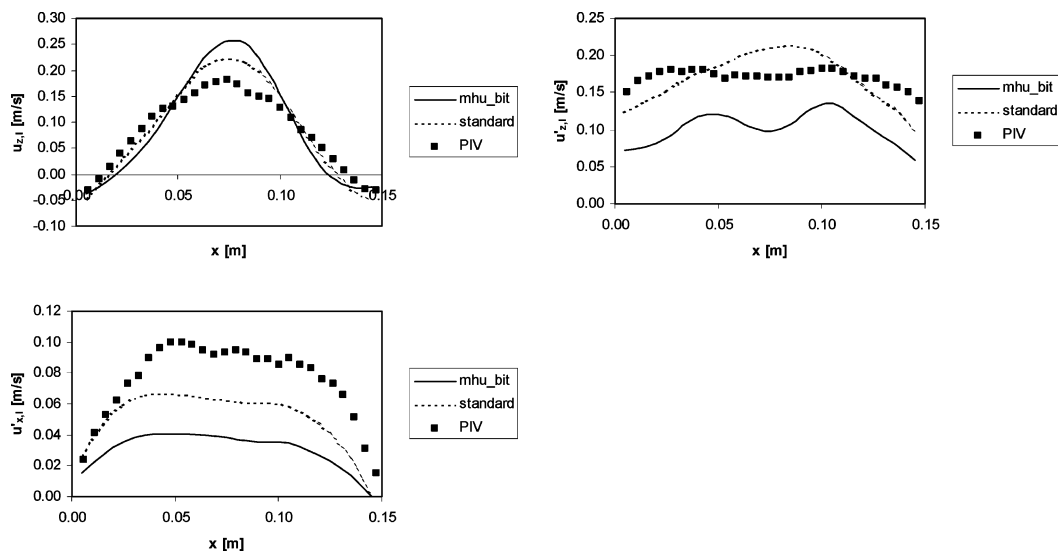


**Figure 10.** Comparison of the simulated and experimental liquid velocity and velocity fluctuations for cases 0 and 5 (see Table 2) at a height of 0.255 m and a depth of 0.075 m. Effect of the bubble-induced turbulence.

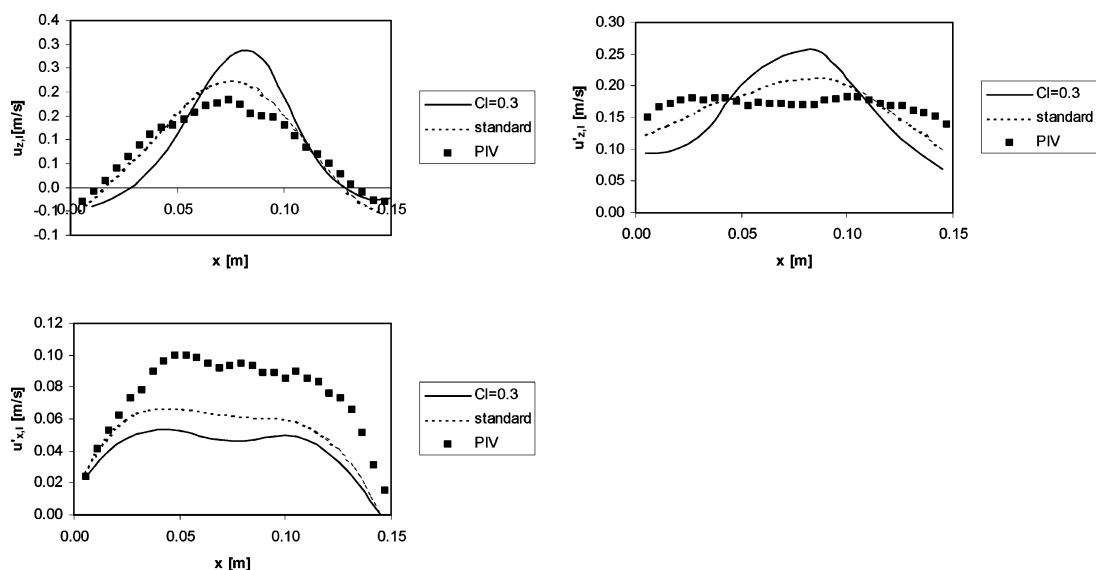


**Figure 11.** Comparison of the simulated and experimental liquid velocity and velocity fluctuations for case 0 and 5 (see Table 2) at a height of 0.255 m and a depth of 0.075 m. Effect of the lift coefficient.

**Table 3. Overview of Different Simulation Cases Coalescence**

case	coalescence model	superficial gas velocity (m/s)
6	Chesters <sup>4</sup>	$2.78 \times 10^{-3}$
7	Lee et al. <sup>5</sup>	$2.78 \times 10^{-3}$
8	Chesters <sup>4</sup>	$1.39 \times 10^{-3}$
9	Chesters <sup>4</sup>	$4.17 \times 10^{-3}$

nounced in the case without turbulence model, which indicates a better prediction of the horizontal plume dynamics.

In case 5 the influence of incorporating bubble-induced turbulence (eq 13) is investigated. Figure 10 shows the simulation results of the average velocity profile and the velocity fluctuations of the cases with and without bubble-induced turbulence. It is seen that the average velocity profiles in the case with bubble-induced turbulence are higher than in the case without bubble-induced turbulence. When the bubble-induced turbulence is incorporated, the effective viscosity is higher than without bubble-induced turbulence. This leads to more dampening of the bubble plume dynamics and to a higher maximum of the average liquid velocity profiles. As a consequence the velocity fluctuations for the horizontal and the vertical direction are lower when bubble-induced turbulence is incorporated.

**5.2. Lift Coefficient.** The value of the lift coefficient in the standard case is 0.5. To study the influence of the lift coefficient, this value is reduced to 0.3, which is the value suggested by Tomiyama.<sup>18</sup> In Figure 11 the results of the average velocity profile and the velocity fluctuations can be seen. It is found that the average velocity profiles in the case of  $C_L = 0.3$  are much higher than in the case of  $C_L = 0.5$ . In the case of  $C_L = 0.3$ , the spreading of the plume is less and therefore the dynamics of the plume are reduced, which leads to a higher average velocity in the center of the column. This observation can also be confirmed by the velocity fluctuations. The velocity fluctuations in the vertical direction in the case with  $C_L = 0.3$  are higher than in the case with  $C_L = 0.5$ . The velocity fluctuations in the horizontal direction are lower in the case with  $C_L = 0.3$ . The observed behavior is in agreement with the findings of Deen et al.,<sup>3</sup> who showed that a lift coefficient of zero leads to a significant overprediction of the liquid velocities in the center of the column. Note that the lift coefficient suggested by Tomiyama<sup>18</sup> results from experiments involving a single bubble. The effect of surrounding bubbles on the lift coefficient is currently not known. As a consequence it is not clear whether the discrepancy between the case with  $C_L = 0.3$  and the experiments can be attributed to an underestimation of the lift force or to the absence of additional forces, such as the turbulent dispersion force.

## 6. Results Breakup and Coalescence

In the DBM the coalescence models of Chesters<sup>4</sup> and Lee et al.<sup>5</sup> were both implemented. In this section the results of the simulations are discussed and compared with experimental data, which were obtained with digital image analysis. The different computational cases are listed in Table 3. In all cases the breakup model of Luo and Svendsen<sup>22</sup> was used.

In our study we used a pseudo 2D bubble column (width, thickness, and height of respectively 0.20, 0.03, and 1.40 m) enabling the application of digital image analysis. The bottom of the column contains a mem-

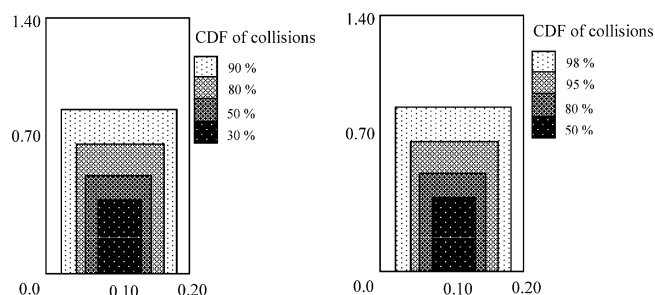


**Figure 12.** Cumulative distribution function of collisions in the bubble column. Left: model of Chesters,<sup>4</sup> case 6. Right: model of Lee et al.,<sup>5</sup> case 7.

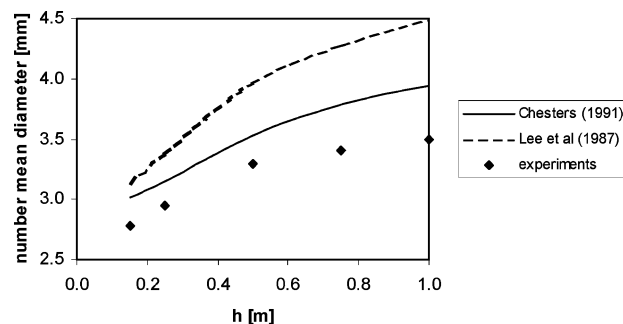


**Figure 13.** Comparison of simulation and experimental results of number mean diameter vs height for cases 6 and 7 (see Table 3).

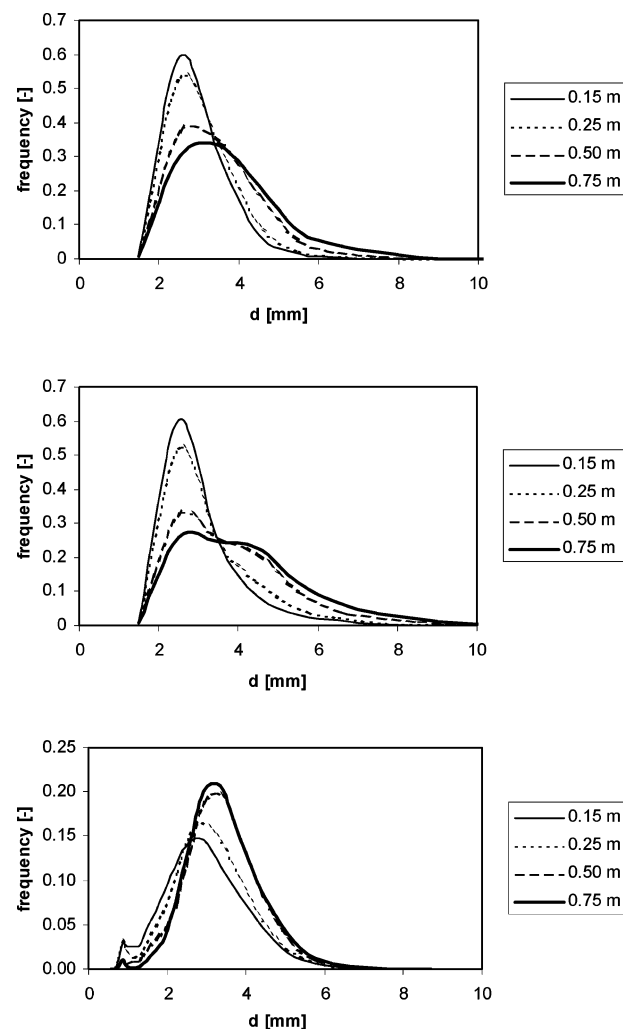


**Figure 14.** Bubble size distribution after 130 s. Top: simulation case 6. Middle: simulation case 7. Bottom: experiments.

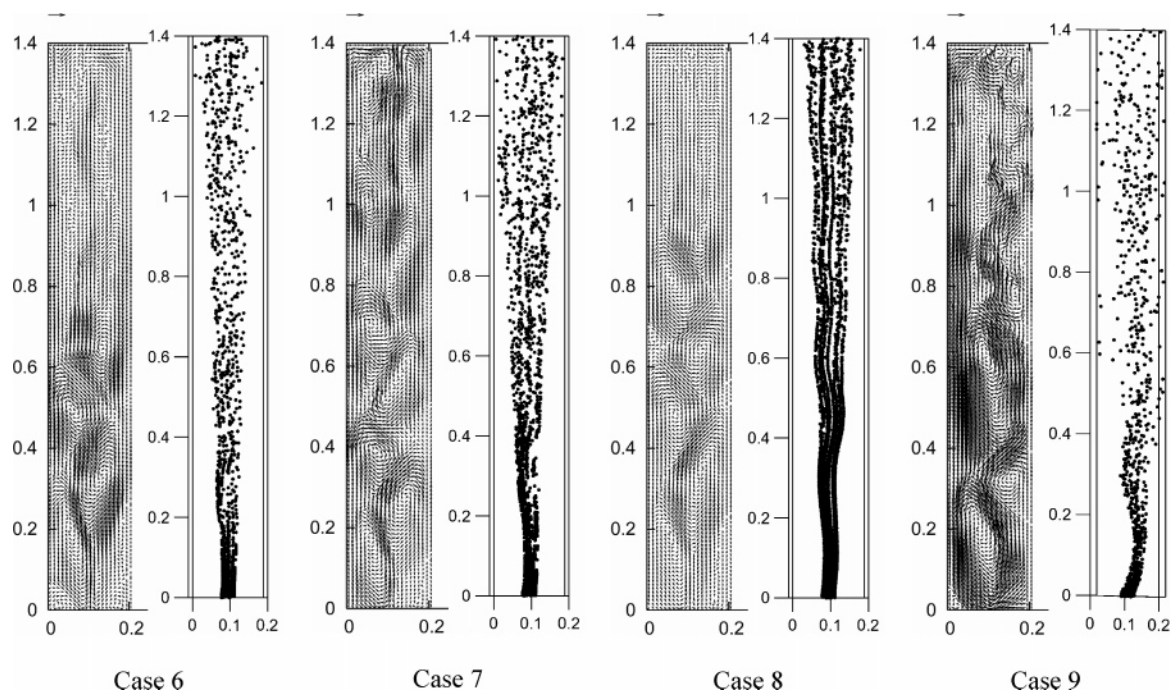


**Figure 15.** Snapshots of the predicted liquid phase velocity (left) and the bubble positions (right) in the center plane of a pseudo 2D column after 70 s. Reference vector =  $0.2 \text{ m s}^{-1}$ .

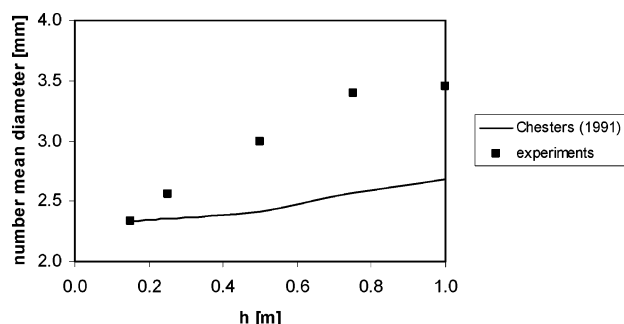


**Figure 16.** Comparison of simulation and experimental results of number mean diameter vs height for case 8 (see Table 3).

brane nozzle with a diameter of 0.02 m. The bubbles leaving the nozzle have a size distribution around 3 mm. This value was used as the initial bubble size in the simulations.

The grid of the computational domain consists of  $20 \times 3 \times 140$  grid cells and the time step is  $1.0 \times 10^{-3} \text{ s}$ . In the simulation the sparger is modeled as eight nozzles in two rows of four nozzles. The distance between the nozzles is 0.01 m. The bubbles are entering the column with a normal bubble diameter distribution. The subgrid scale model is used to model the turbulent fluctuations at the subgrid scale. Each case was simulated for 130 s, which appears to be sufficient, as was found in the previous section.

The simulation results of the two coalescence models are compared with the experimental data in terms of the bubble size distribution. For comparison with experimental data, the bubble distribution is divided in 10 bubble size classes. Furthermore, the number mean diameter is calculated at four different heights of the column. The number mean diameter is the average diameter of all bubbles in the sample and is given as follows:

$$d_{10} = \frac{1}{N_B} \sum_{i=1}^{N_B} d_i \quad (20)$$

Two important parameters for coalescence to occur are the collision frequency and the coalescence efficiency. The collision frequency is determined by the DBM. For every collision the coalescence efficiency is calculated. It was found that in the simulations for the coalescence model of Chesters<sup>4</sup> (case 6) 43% of all collision results in coalescence.

As can be seen in Figure 12, most of the collisions and thus of the coalescence occur in the lower part of the column because in this part the bubbles stay together in a plume. In the upper part of the column the bubbles are more homogeneously distributed over the cross sectional area of the column and the chance for collision is smaller.

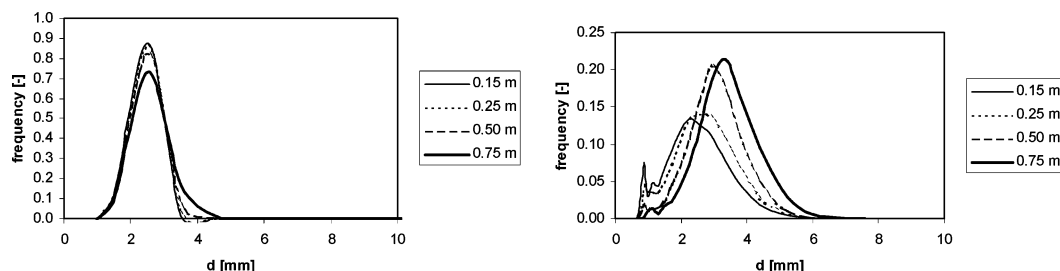


**Figure 17.** Bubble size distribution for case 8 after 130 s. Left: simulation. Right: experiment.

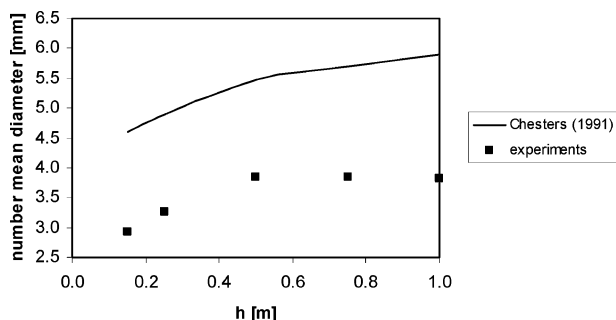


**Figure 18.** Comparison of simulation and experimental results of number mean diameter vs height for case 9 (see Table 3).

When the model of Lee et al.<sup>22</sup> is used, 85% of all collisions result in coalescence. Most coalescence occurs in the lower part of the column, in the same area as in the model of Chesters.<sup>4</sup>

Figure 13 shows the number mean diameter as a function of the height in the column. Both in the simulations and the experiments it is found that the mean diameter increases with increasing height in the column. This is due to the fact that the higher their position in the column, the longer bubbles generally have resided in the column and the more opportunity they had to coalesce. The difference in mean diameter between the simulation results of model of Chesters<sup>4</sup> and the experiments is on the order of 15%. For the model of Lee et al.<sup>5</sup> the difference is around 35%.

In Figure 14 the bubble size distribution at different heights in the column for the simulations and the experiments are shown. As can be observed in this figure, the bubble size distribution moves to larger diameters, with increasing height. Contrary to the experiments, the bubble size distribution predicted by the simulations widens with increasing height in the column.

In both models the mean diameter is overpredicted, probably due to the fact that hardly any breakup occurs. The coalescence model of Chesters<sup>4</sup> combined with the breakup model of Luo and Svendsen<sup>22</sup> appears to give the best results.

Figure 15 shows snapshots of the predicted liquid phase velocity fields and the bubble positions for all the simulated cases. It can be seen that in all cases the flow is driven by a bubble plume, which moves through the column in an oscillatory manner. The total number of bubbles present in the column is less when the coalescence model of Lee et al.<sup>5</sup> is used, due to the higher coalescence efficiency. In both the simulations and the experiments it is observed that the bubble plume tends to spread over the width of the column, at higher positions in the column.

In case 8 the model of Chesters<sup>4</sup> is used with a lower superficial gas velocity ( $1.39 \times 10^{-3} \text{ m s}^{-1}$ ). The number

of collisions between two bubbles that result in coalescence (i.e., the coalescence efficiency) at a lower superficial gas velocity is the same as for case 6. Most of the coalescence occurs in the lower part of the column ( $<0.70 \text{ m}$ ).

For case 8, the bubbles stay closer together in a plume, as can be seen in Figure 15. Compared to the experimental results and the case with higher superficial velocity (i.e., case 6) the number of collisions and consequently the coalescence rate is lower at lower superficial velocity. It is observed that the bubbles in the plume are rising in lines behind each other. This is most probably related to the absence of a model for the bubble-wake interaction.

Figure 16 shows the number mean diameters for different heights in the column. The predicted mean diameters are smaller than those in the experiments. Furthermore, the bubble size distribution of case 8, as shown in Figure 17 is narrower and the maximum of the distribution is found at a smaller bubble diameter than in case 6.

In case 9 the model of Chesters<sup>4</sup> is used at a higher superficial gas velocity ( $4.17 \times 10^{-3} \text{ m s}^{-1}$ ) compared to case 6. The number of collisions between two bubbles that result in coalescence is the same as in the two other cases employing the model of Chesters.<sup>4</sup>

In Figure 15 it can be seen that in the lower part of the column the bubbles stay together in a plume. The bubbles are close together and they collide and subsequently coalesce very often. In the upper part of the column, the bubbles are spread over the entire width of the column, which results in a reduced coalescence rate.

The number mean diameter for case 9 is presented in Figure 18. When this case is compared with those at other flow rates, it turns out that the mean diameter increases with increasing flow rate. This can be explained by the fact that at higher flow rates, the gas fraction increases, which leads to an increased collision frequency. The differences between the simulated and measured mean diameters are higher for case 9 than for case 6. This is probably due to the fact that despite the increased turbulence hardly any breakup occurs.

The bubble size distribution of case 9 is shown in Figure 19. It is found that similar to case 6, the predicted bubble size distribution is too wide and the maximum is found at too large bubble diameters.

## 7. Discussion and Conclusions

In this work a discrete bubble model (DBM) was used to investigate the hydrodynamics, coalescence and breakup occurring in bubble columns. The 3D DBM code, originally developed by Delnoij et al.,<sup>1-2</sup> was extended to incorporate models describing the coales-

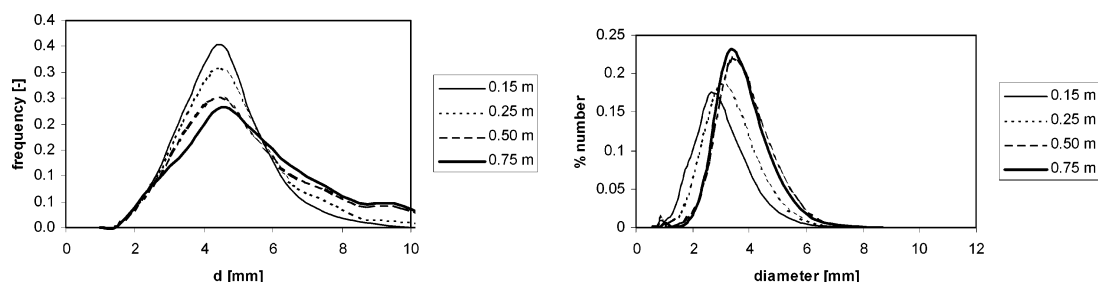


**Figure 19.** Bubble size distribution for case 9 after 90 s. Left: simulation. Right: experiment.



cence and breakup along with a subgrid scale closure model for the turbulence.

Simulation results of the DBM including the subgrid scale model are compared to experimental PIV data measured by Deen et al.<sup>3</sup> for the case of a square cross-sectioned column. The mean and fluctuating velocities predicted in the simulations show good agreement with the experimental data. It was found that the simulations are relatively insensitive to changes in time step or grid size.

Without the use of a subgrid scale model, the average velocity and velocity fluctuations of the liquid phase are much lower than in the case with subgrid scale model. This is due to the lower effective viscosity in this case, which leads to less dampening of the bubble plume dynamics and subsequently to flatter mean liquid velocity profiles. The opposite effect is observed when bubble-induced turbulence is accounted for. In this case the effective viscosity is increased. Furthermore, it was found that the influence of the subgrid scale velocity is negligible.

When the lift coefficient is reduced from 0.5 to 0.3, the average velocity and velocity fluctuations are much higher. In the case of a smaller lift coefficient the spreading of the plume is less and therefore the dynamics of the plume are reduced, which leads to overprediction of the average velocity in the center of the column.

The best results are obtained when a subgrid scale model is incorporated, using a time step of  $0.5 \times 10^{-3}$  s, a grid size of 0.01 m and a lift coefficient of 0.5.

The DBM was extended with the coalescence model of Chesters<sup>4</sup> and Lee et al.<sup>5</sup> and the breakup model of Luo and Svendsen.<sup>22</sup> The bubble size distributions that were predicted with the different submodels are compared to experimental data that were measured in a pseudo 2D bubble column with an air–water system.

The breakup model of Luo and Svendsen<sup>22</sup> was originally developed for energy dissipation rates larger than  $0.5 \text{ m}^2 \text{ s}^{-3}$ . However, in bubble columns operated at low gas flow rates and low turbulence intensities the energy dissipation rate is in the order of  $10^{-2} \text{ m}^3 \text{ s}^{-1}$ . For these values of the energy dissipation rate the breakup model predicts hardly any breakup. In the simulations, breakup only occurs in the top of the column, when the energy dissipation is larger than  $10^{-1} \text{ m}^3 \text{ s}^{-1}$  and the bubble diameter sufficiently large ( $>5$  mm).

The number of collisions between two bubbles that result in coalescence is 43% with the coalescence model of Chesters<sup>4</sup> and 85% with the coalescence model of Lee et al.,<sup>5</sup> irrespective of the superficial gas velocity. Most of the coalescence occurs in the lower part of the column. When either of the coalescence models is used, the mean diameter is overpredicted, due to the underprediction of the breakup. The results of the coalescence model of Chesters<sup>4</sup> combined with the breakup model of Luo and Svendsen<sup>22</sup> shows the best correspondence to the experimental data.

For increasing superficial gas velocities the number of collisions and consequently the coalescence rate increases. Further research is required to resolve the differences between the experiments and the simulations. In our view, special attention should be paid to the breakup model.

## Literature Cited

- (1) Delnoij, E.; Lammers, F. A.; Kuipers, J. A. M.; Van Swaaij, W. P. M. Dynamic simulation of dispersed gas–liquid two-phase flow using a discrete bubble model. *Chem. Eng. Sci.* **1997**, *52*, 1429–1458.
- (2) Delnoij, E.; Kuipers, J. A. M.; Van Swaaij, W. P. M. A three-dimensional CFD model for gas–liquid bubble columns. *Chem. Eng. Sci.* **1999**, *54*, 2217–2226.
- (3) Deen, N. G.; Solberg, T.; Hjertager, B. H. Large eddy simulation of the gas–liquid flow in a square cross-sectioned bubble column. *Chem. Eng. Sci.* **2001**, *56*, 6341–6350.
- (4) Chesters, A. K. The modelling of coalescence processes in fluid–liquid dispersions: a review of current understanding. *Trans. IChemE* **1991**, *69*, 259–270.
- (5) Lee, C.-H.; Erickson, L. E.; Glasgow, L. A. Bubble breakup and coalescence in turbulent gas–liquid dispersion. *Chem. Eng. Commun.* **1987**, *59*, 65–84.
- (6) Sokolichin, A.; Eigenberger, G.; Lapin, A.; Lübbert, A. Dynamic numerical simulation of gas–liquid two-phase flows. Euler/Euler versus Euler/Lagrange. *Chem. Eng. Sci.* **1997**, *52*, 611–626.
- (7) Sokolichin, A.; Eigenberger, G. Applicability of the standard  $k-\epsilon$  turbulence model to the dynamic simulation of bubble columns: Part i. Detailed numerical simulations. *Chem. Eng. Sci.* **1999**, *54*, 2273–2284.
- (8) Lapin, A.; Lübbert, A. Numerical simulation of the dynamics of two-phase gas–liquid flows in bubble columns. *Chem. Eng. Sci.* **1994**, *49*, 3661–3674.
- (9) Trapp, J. A.; Mortensen, G. A. A discrete particle model for bubble slug two phase flow. *J. Comput. Phys.* **1993**, *107*, 367–377.
- (10) Laín, S.; Bröder, D.; Sommerfeld, M. Numerical simulations of the hydrodynamics in a bubble column: quantitative comparisons with experiments. *Int. Conf. Multiphase Flow*, 4th **2001**.
- (11) van Sint Annaland, M.; Deen, N. G.; Kuipers, J. A. M. Multi-Level Modelling of Dispersed Gas–Liquid Two-Phase Flows. In *Series: Heat and Mass Transfer*; Sommerfeld, M., Eds.; Springer-Verlag: Berlin, 2003; pp 139–157.
- (12) Deen, N. G.; van Sint Annaland, M.; Kuipers, J. A. M. Multi-scale modeling of dispersed gas–liquid two-phase flow. *Chem. Eng. Sci.* **2004**, *59*, 1853–1861.
- (13) Buwa, V. V.; Ranade, V. V. Dynamics of gas–liquid flow in a rectangular bubble column: experiments and single/multi-group CFD simulations. *Chem. Eng. Sci.* **2002**, *57*, 4715–4736.
- (14) Lo, S. Application of population balance to CFD modeling of bubbly flows via the MUSIG model, 1998, AEAT-1096, CFX International, AEA Technology, U.K.
- (15) Lehr, F.; Millies, M.; Mewes, D., Bubble-Size Distributions and Flow Fields in Bubble Columns. *AIChE J.* **2002**, *48*, 2426–2443.
- (16) Sommerfeld, M.; Bourloutski, E.; Bröder, D. Euler/Lagrange calculations of bubbly flows with consideration of bubble coalescence. *Can. J. Chem. Eng.* **2003**, *81*, 508–518.
- (17) Auton, T. R. The dynamics of bubbles, drops and particles in motion in liquids. Ph.D. Thesis, University of Cambridge, Cambridge, U.K., 1983.
- (18) Tomiyama, A. 1998, Struggle with computational bubble dynamics. *Int. Conf. Multiphase Flow*, 3rd **1998**.
- (19) Sato, Y.; Sekoguchi, K. Liquid velocity distribution in two-phase bubble flow. *Int. J. Multiphase Flow* **1975**, *2*, 79–95.
- (20) Smagorinsky, J. General circulation experiments with the primitive equations. *Mon. Weather, Rev.* **1963**, *91*, 99–165.
- (21) Mason, P. J.; Callen, N. S. On the magnitude of the subgrid-scale eddy coefficient in large-eddy simulations of turbulent channel flow. *J. Fluid Mech.* **1986**, *162*, 439–462.
- (22) Luo, H.; Svendsen, H. F. Theoretical model for drop and bubble breakup in turbulent dispersions. *AIChE J.* **1996**, *42*, 1225–1233.
- (23) Darmana, D.; Deen, N. G.; Kuipers, J. A. M. Detailed Modeling of Hydrodynamics, Mass transfer and Chemical Reactions in a Bubble Column using a Discrete Bubble Model. *Chem. Eng. Sci.*, in press.

(24) Centrella, J.; Wilson, J. R. Planar numerical cosmology. II. The difference equations and numerical tests. *Astrophys. J. Suppl. Ser.* **1984**, *54*, 229–249.

(25) Hawley, J. F.; Smarr, L. L.; Wilson, J. R. A numerical study of nonspherical black hole accretion. II. Finite differencing and code calibration. *Astrophys. J. Suppl. Ser.* **1984**, *55*, 211–246.

(26) Goldschmidt, M. J. V. Hydrodynamic modelling of fluidised bed spray granulation. Ph.D. Thesis, University of Twente, Enschede, The Netherlands, 2001.

(27) Kuipers, J. A. M.; van Duin, K. J.; van Beckum, F. P. H.; van Swaaij, W. P. M. Computer simulation of the hydrodynamics of two-dimensional gas-fluidized bed. *Comput. Chem. Eng.* **1993**, *17*, 839–858.

*Received for review* August 19, 2004

*Revised manuscript received* December 22, 2004

*Accepted* December 29, 2004

IE0492449